



JWST Reveals Widespread CO Ice and Gas Absorption in the Galactic Center Cloud G0.253+0.016

Adam Ginsburg¹ , Ashley T. Barnes² , Cara D. Battersby³ , Alyssa Bulatek¹ , Savannah Gramze¹ , Jonathan D. Henshaw^{4,5} , Desmond Jeff¹ , Xing Lu⁶ , E. A. C. Mills⁷ , and Daniel L. Walker⁸

¹ Department of Astronomy, University of Florida, P.O. Box 112055, Gainesville, FL, USA

² European Southern Observatory (ESO), Karl-Schwarzschild-Straße 2, D-85748 Garching, Germany

³ University of Connecticut, Department of Physics, 196A Auditorium Road, Unit 3046, Storrs, CT 06269, USA

⁴ Astrophysics Research Institute, Liverpool John Moores University, 146 Brownlow Hill, Liverpool L3 5RF, UK

⁵ Max-Planck-Institut für Astronomie, Königstuhl 17, D-69117 Heidelberg, Germany

⁶ Shanghai Astronomical Observatory, Chinese Academy of Sciences, 80 Nandan Road, Shanghai 200030, People's Republic of China

⁷ Department of Physics and Astronomy, University of Kansas, 1251 Wescoe Hall Dr., Lawrence, KS 66045, USA

⁸ UK ALMA Regional Centre Node, Jodrell Bank Centre for Astrophysics, The University of Manchester, Manchester M13 9PL, UK

Received 2023 August 2; revised 2023 September 14; accepted 2023 September 14; published 2023 December 4

Abstract

We report JWST NIRCам observations of G0.253+0.016, the molecular cloud in the Central Molecular Zone known as “The Brick,” with the F182M, F187N, F212N, F410M, F405N, and F466N filters. We catalog 56,146 stars detected in all six filters using the `crowdsourc` package. Stars within and behind The Brick exhibit prodigious absorption in the F466N filter that is produced by a combination of CO ice and gas. In support of this conclusion, and as a general resource, we present models of CO gas and ice and CO₂ ice in the F466N, F470N, and F410M filters. Both CO gas and ice contribute to the observed stellar colors. We show, however, that CO gas does not absorb the Pfβ and H ϵ lines in F466N, but that these lines show excess absorption, indicating that CO ice is present and contributes to observed F466N absorption. The most strongly absorbed stars in F466N are extinguished by ~ 2 mag, corresponding to $>80\%$ flux loss. This high observed absorption requires very high column densities of CO, and thus a total CO column that is in tension with standard CO abundance and/or gas-to-dust ratios. This result suggests the CO/H₂ ratio and dust-to-gas ratio are greater in the Galactic Center than in the Galactic disk. Ice and/or gas absorption is observed even in the cloud outskirts, implying that additional caution is needed when interpreting stellar photometry in filters that overlap with ice bands throughout galactic centers.

Unified Astronomy Thesaurus concepts: [Infrared dark clouds \(787\)](#); [Ice composition \(2272\)](#)

1. Introduction

G0.253+0.016, also known as “The Brick,” is among the best-studied infrared dark clouds in the Galaxy (Lis et al. 1991; Lis & Carlstrom 1994; Lis et al. 1994, 2001; Lis & Menten 1998; Longmore et al. 2012; Clark et al. 2013; Kauffmann et al. 2013; Rodríguez & Zapata 2013; Rathborne et al. 2014a, 2014b, 2015; Bally et al. 2014; Johnston et al. 2014; Pillai et al. 2015; Federrath et al. 2016; Marsh et al. 2016; Walker et al. 2016; Henshaw et al. 2019, 2022; Petkova et al. 2023). It is well known for being dense and turbulent (Clark et al. 2013; Rathborne et al. 2015; Federrath et al. 2016; Mills et al. 2018; Henshaw et al. 2019, 2020) while exhibiting few signs of star formation, much less than is typical for such a massive cloud (Longmore et al. 2012; Rodríguez & Zapata 2013; Mills et al. 2015; Walker et al. 2016, 2021). Several explanations have been offered for its relatively poor star formation: that it is young (Kruijssen et al. 2015; Henshaw et al. 2016), that it is highly turbulent (Federrath et al. 2016), that it is supported by magnetic fields (Pillai et al. 2015), and that it is many clouds along the line of sight (Henshaw et al. 2019, 2022). Each of these explanations is likely to play some role in the cloud’s state and evolution.

Gas in the Galactic Center is notably different from gas seen elsewhere in our Galaxy. It is richer in complex molecules (Jones et al. 2012) and warmer (Ao et al. 2013; Ginsburg et al. 2016; Krieger et al. 2017). Despite high gas temperatures, the dust in the Central Molecular Zone (CMZ) is not terribly warm (Tang et al. 2021), so ice can accumulate on dust grains. Ice has long been seen in mid-infrared spectra of sources in the Galactic Center (Lutz et al. 1996; Chiar et al. 2000; Moneti et al. 2001), as has CO gas. Toward Sgr A*, ice comprises a minority ($<10\%$) of the CO, which is dominated instead by gas, as expected given the high gas temperatures and extreme velocity dispersion of gas in the inner parsec (Moneti et al. 2001; Moultaika et al. 2009). Beyond the inner parsec, though, the ice properties of the Galactic Center are little explored. A handful of Infrared Space Observatory spectra were taken toward various positions, revealing both CO₂ and CO ice features, but little has been written about them. An et al. (2011) and Jang et al. (2022) used spectra from the Spitzer IRS to show that CO₂ ice is common toward massive young stellar objects in the Galactic Center, and that CO₂ is present in both gas and ice phases.

More generally, ice is observed throughout the molecular interstellar medium (Boogert et al. 2015). However, ice is much more poorly studied than gas in the interstellar medium because observable ice features occur only in the infrared, either in narrow bands that are difficult to observe from the ground (e.g., Günay et al. 2020, 2022) or in bands that are only observable from space. The majority of published ice studies use spectroscopy, not photometry, in large part because the effects of ice on broadband filters (e.g., Spitzer’s IRAC) are



Original content from this work may be used under the terms of the [Creative Commons Attribution 4.0 licence](#). Any further distribution of this work must maintain attribution to the author(s) and the title of the work, journal citation and DOI.

Table 1
Observations

Filter Name	rms Offset (arcsec)	90th Percentile Mag. (AB)	Number of Sources
F182M	0.020	19.0	337,561
F187N	0.021	18.8	213,894
F212N	0.020	17.8	236,077
F405N	...	16.6	85,126
F410M	0.016	16.6	102,344
F466N	0.021	16.3	79,629

Note. The rms offset reports the standard deviation of the difference in source position between the specified filter and the reference filter, F405N. The 90th percentile column reports the 90th percentile magnitude in the catalog to give a general sense of depth.

usually small. The wide range of medium- and narrowband filters on JWST NIRCcam change the state of the field, enabling extensive broad-field ice study through photometry.

We present JWST observations in narrowband filters toward The Brick, highlighting the first striking result that CO ice is widespread. In Section 3, we describe the data processing and catalog creation. Section 4 describes the measurements of both star colors (Section 4.1) and diffuse gas emission (Section 4.2), then describes models of absorption by both CO gas (Section 4.3) and ice (Section 4.4) that explain some of the observed colors. We briefly discuss these results in Section 5 and then conclude in Section 6. All of the analysis tools, including the notebooks used to make the figures in this document, are made available through a GitHub repository⁹ and with a static version in a Zenodo repository (Ginsburg & Gramze 2023).

2. Observations

Observations were taken on 2022 August 28 as part of JWST program 2221 in visit 001. The data presented in this paper were obtained from the Mikulski Archive for Space Telescopes (MAST) at the Space Telescope Science Institute (STScI). The specific observations analyzed can be accessed via [10.17909/2ffq-e139](https://doi.org/10.17909/2ffq-e139). This program consists of two observations focused on The Brick, with coordinated parallel observations performed toward CMZ Cloud C. We present only the NIRCcam observations of The Brick in this work; the MIRI observations of The Brick and NIRCcam and MIRI observations of Cloud C will be presented in future works. We obtained images in six filters listed in Table 1. We observed in narrowband filters in order to measure the extended line emission from hydrogen recombination lines (Pa α , Br α , Pf β) and to search for outflows (H₂ in F212N) and hot CO emission from disks (F466N). The GTO program 1182 has observed approximately the same field in broadband filters.

In the NIRCcam data we present, each image comprises 24 exposures taken in the 6-TIGHT FULLBOX mosaic strategy,¹⁰ with six independent positions and four subpixel dithers per position. Frames were read out in BRIGHT-2 mode with two groups per integration for a total exposure time of 1031 s.¹¹

⁹ <https://github.com/keflavich/brick-jwst-2221/>

¹⁰ <https://jwst-docs.stsci.edu/jwst-near-infrared-camera/nircam-operations/nircam-dithers-and-mosaics/nircam-primary-dithers>

¹¹ <https://jwst-docs.stsci.edu/jwst-near-infrared-camera/nircam-instrumentation/nircam-detector-overview/nircam-detector-readout-patterns>

3. Data Processing

We downloaded the data from the MAST archive using `astroquery` (Ginsburg et al. 2019; Basseur et al. 2020). We reprocessed data starting from L2 products, i.e., the `cal` files, which include 24 individual flux-calibrated frames for each filter.

Our reduction code is provided on GitHub.¹²

3.1. Frame-matching Astrometry

Images were processed with a slightly modified version of the JWST pipeline based on version 1.11.1 (Bushouse et al. 2023). The `tweakreg` command was run on long-wavelength NIRCcam data using the VISTA variables in the Vía Láctea (VVV) DR2 catalog (Saito et al. 2012) as an astrometric reference instead of the Gaia catalog (there were too few stars detected in common by both Gaia and JWST, and most were saturated). We then created a reference catalog based on the F405N catalog, which had fewer saturated bright stars than F410M and therefore more good associations with the ground-based near-infrared data. In the `make_reftable.py` script, we cut the F405N catalog based on `crowdsourcing` quality flags (`qf > 0.95`, `spread < 0.25`, `frac > 0.9`). This reference catalog was then used as the input to `tweakreg` for the other filters. We found that the `tweakreg` pipeline did not adequately correct the image registration to the absolute coordinates we provided, so we manually cross-matched the catalogs and computed shifts using the `realign_to_catalog` and `merge_a_to_b` functions in `align_to_catalogs.py`.

3.2. 1/f Noise Removal

The narrowband filters, particularly F187N, F212N, and F466N, exhibited significant “streaking” noise that is strongly evident in the low-signal regions of the image, i.e., the majority of the molecular cloud. This streaking was caused by $1/f$ noise in the detectors (STScI helpdesk ticket INC0181624). As a first preprocessing step, we performed “destreaking” on each detector following a method suggested by Massimo Robberto (private communication), in which:

1. Each detector was split into four horizontal quadrants with width 512 pixels and height 2048 pixels.
2. The median across the horizontal axis was calculated, resulting in a 2048 pixel array.
3. In a slight departure from Massimo’s method, we then smoothed the median array using a 1D median filter with length that varied depending on the filter. ‘F410M’: 15, ‘F405N’: 256, ‘F466N’: 55, ‘F182M’: 55, ‘F187N’: 256, ‘F212N’: 512. We found that the original method, which was to obtain a single constant at this step, turned the destreaking process into a high-pass filter and therefore removed significant extended emission.
4. We subtracted the median array from each quadrant, then added back the smoothed median.

We evaluated the effectiveness of this process by eye. While the original destreaker completely removed the $1/f$ horizontal features, it also removed all of the extended background. The modified version removed most of the horizontal features while preserving the large-scale extended structure. It is likely that

¹² https://github.com/keflavich/brick-jwst-2221/releases/tag/resubmission_20230903; DOI: 10.5281/zenodo.8313307

some intermediate-scale features (i.e., physical features comparable to 512 pixels across) are not recovered by this procedure, which will need to be accounted for in analysis of the extended emission.

3.3. Photometric and Astrometric Cataloging

For photometry of unsaturated stars, we used the `crowd-source` python package (Schlafly 2021). We used a point-spread function (PSF) model from `webbpsf` (Perrin et al. 2015). Because we were using mosaicked images, the `webbpsf` PSF is not a perfect representation of the data; each individual frame had to be shifted and drizzled to form our final images. We therefore used the `webbpsf` model smoothed by a small amount, 0.05 pixels, as our PSF. We experimented with other PSFs and found that this approach was good enough, but it is not quantitatively optimal. Furthermore, for the short-wavelength bands, we adopted the PSF for a single detector (NRCA1 or NRCB1 as appropriate) for the full frame, since `webbpsf` does not provide a tool to produce a PSF grid across the whole module.

We identified saturated stars so that we could ignore them, and stars too close to them (which are likely to be affected by the extended PSFs of saturated stars), for further analysis. To identify these stars, we measured the centroids of all regions in which either the data (FITS extension `SCI`) or the variance (FITS extension `VAR_POISSON`) was zero. We then fitted the PSF of these stars excluding the saturated pixels and a surrounding set of pixels identified through binary dilation. The detailed values of the dilation size are given in `saturated_star_finding.py`. While we measured both photometry and astrometry of these saturated stars, we use only the astrometry in subsequent sections, and only as a means to automatically exclude saturated stars and their nearest neighbors.

3.4. Catalog Matching

We assembled a catalog consisting of all sources found in any of our six filters. To assemble the coordinate list, we started with all coordinates in the F405N catalog, then for each other filter, we added all sources that did not have a match in the existing catalog within $d < 0''.15$. The cross-match shows a large peak for matches within $d < 0''.1$ with large tails at greater separation; we have not investigated the origin of these large-offset sources, but suspect low signal-to-noise sources, PSF artifacts, and features in the extended background may contribute. We then excluded all sources with a cross-match distance to the reference filter’s coordinates $d > 0''.1$ (the reference filter is F405N by default, but for sources with nondetections in F405N, a different reference filter was adopted).

For subsequent analysis, we then rejected all sources with magnitude errors $\sigma_m > 0.1$, “quality factor” $qf \leq 0.6$, $\text{spread} > 0.25$, or $\text{fracflux} < 0.8$, all of which are values calculated by `crowdsources`. These choices select for round, pointlike, unblended stars. We also limited our analysis to sources with detections in all six bands.

The resulting cross-matched catalogs had rms positional offsets $< 0''.02$ (Table 1). We do not concern ourselves further with astrometry in this manuscript, but caution that, with these sizeable cross-match errors, our catalogs likely are not yet of sufficient quality to support measurements of proper motion.

We found 377,236 stars with a good measurement in at least one filter, and 56,146 with good measurements in all six filters.

The number of good measurements found in each filter is given in Table 1 (these include sources with offsets from the reference filter $d > 0''.1$).

3.5. Starless Image Creation

For comparison of star locations to extinction features, we preferred to work with an image with stars removed. Note that, because of significant uncertainty in this process, we have used the star-subtracted images only for qualitative, not quantitative, analysis. A starless image is the natural residual of an image that has been processed through a PSF photometry routine that appropriately accounts for the non-point-source background. However, when we produced such images, they had substantial residual features, which were caused by a combination of an imperfect PSF model and oversubtraction of sources on extended backgrounds. To create a cleaner starless image, we took the difference between the narrowband and medium-band images after appropriately scaling the narrowband image. The F405N image was convolved with a 0.3 pixel Gaussian to better match the PSF of the F410M filter.

We produced a line-free F410M image, labeled 410m405, by using the following equation:

$$S_{410m405} = \frac{S_{F410M} - S_{F405N} \times w}{1 - w} \quad (1)$$

where w is the fractional bandwidth of F410M covered by F405N and $S_{\text{filtername}}$ is the surface brightness in a given filter. This process effectively creates a continuum-only “notch” filter image. We produced a star-free F405N image, labeled 405m410, by subtracting the (theoretically continuum-only) 410m405 image from F405N. Note that the images are in units of surface brightness, MJy sr^{-1} , such that line emission in broadband filters is diluted (will have a lower surface brightness), while spectrally flat continuum sources (to a coarse approximation, stars) will have the same brightness in broad and narrow filters. We then produced a somewhat star-free F466N image, which we label 466m410, by subtracting the 410m405 image scaled by $R = (4.66/4.10)^{-2} = 0.77$ (assuming a blackbody on the Rayleigh–Jeans tail, $S_\lambda \propto \lambda^{-2}$).

$$S_{466m410} = S_{F466N} - S_{410m405} \times R. \quad (2)$$

This $S_{466m410}$ image has much greater residuals, since the wavelengths do not overlap and differences in dust extinction (and ice absorption; see below) render the subtraction somewhat poor. Nevertheless, the stars are largely removed, and in particular, their extended PSFs are mitigated. The subtraction process is recorded in the notebooks

```
BrA_separation_nrca.ipynb,
BrA_separation_nrcb.ipynb,
F466N_separation_nrca.ipynb,
and F466N_separation_nrca.ipynb.
```

This process still left significant residuals throughout both the 405m410 and 466m410 images. To further remove stars—at this stage, purely for aesthetic purposes—we identified the locations of significant residuals and masked them out, then interpolated across them. We performed this process iteratively, using larger masks for stars with more extended PSF features and smaller masks for more compact, fainter stars. The details of the process were largely decided “by hand,” i.e., testing a

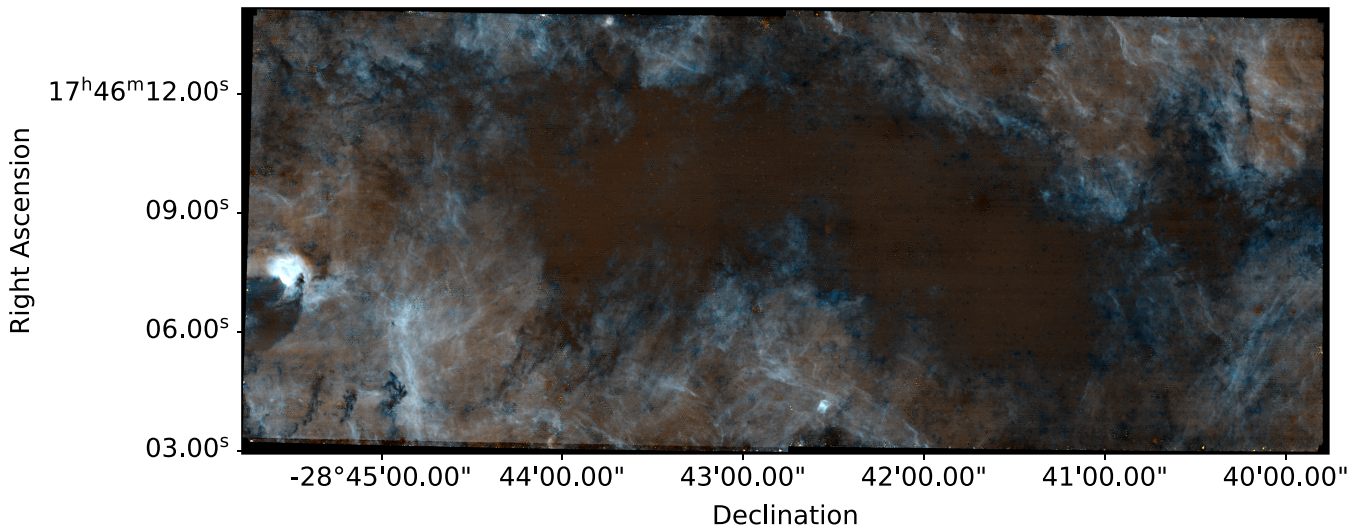


Figure 1. The full-field star-subtracted image as described in Section 3.5. This image captures extended recombination line emission from $\text{Pf}\beta$ and $\text{H}\epsilon$ in F466N (466m410, continuum-subtracted F466N, is shown in red) and $\text{Br}\alpha$ in F405N (405m410, continuum-subtracted F405N, is shown in blue), highlighting The Brick as the dark cloud spanning the image. The green channel is the sum of the red and blue channels and therefore adds no information. Most of the extended emission is approximately white because both the F466N and F405N filters contain recombination lines ($\text{Pf}\beta + \text{H}\epsilon$ and $\text{Br}\alpha$, respectively). The color is more red when dust extinction is the dominant absorption effect and more blue when CO absorption is dominant (see Section 4.2), but the colors should not be interpreted quantitatively. Note that significant artistic license has been taken to fill in regions where star PSFs have made pixel fluxes unrecoverable; the image represents the overall structure of the cloud well, but many small-scale features are artifacts of the star subtraction. Note that decl. is on the x -axis, contrary to convention. A full-resolution version is available online.

small variation in a parameter (e.g., the mask size) and revising if it did not look good. We also created custom masks to remove residuals from extended PSFs. The masking process is recorded in the `StarDestroyer_nrca.ipynb` and `StarDestroyer_nrbc.ipynb` notebooks. After each module was fully star-subtracted, the images were merged in the `Stich_A_to_B.ipynb` notebook.

Figure 1 shows the merged full-frame image. The color choices were made only for aesthetic reasons. Figure 2(a) shows the same image, and Figure 2(b) shows the version with stars before removal. Figure 2 also shows a subset of the cataloged stars as green and blue X's, as will be described in Section 4.1.

4. Results

The Brick stands out in infrared images as a dark feature against a background both of stars and of diffuse emission (e.g., Figure 1). We start by highlighting in Section 4.1 that The Brick is an extinction feature, but that it exhibits peculiar colors in the F466N filter. We then discuss the diffuse emission from recombination lines in Section 4.2. Both from absorption of this diffuse emission and from the colors of extinguished stars, we infer that gas (Section 4.3) and ice (Section 4.4) are contributing to the line-of-sight absorption that defines The Brick. This physical explanation is summarized in Figure 3, which shows the atomic and molecular lines and the ice bands overlaid on the observed filters. The observational result is summarized in Figure 4, which shows the photometric data.

4.1. Some Stars Are Too Blue in F466N Colors

The first intriguing result from these data is that, in colors including F466N, which is our longest-wavelength filter, the stars that are most extinguished appear too blue. In general, dust extinction causes reddening, i.e., the shorter-wavelength photons are more attenuated than the long-wavelength photons; in this case, we see the inverse effect happening. This feature is evident in color–magnitude and color–color diagrams (CMDs

and CCDs; Figure 4). Figure 4(c) shows a CCD with an extinction vector from Chiar & Tielens (2006, hereafter CT06) overlaid,¹³ demonstrating that colors including the F466N filter go in a direction not accounted for by normal dust-extinction-driven reddening. We see excess absorption in the F466N filter of roughly 0.035 magnitudes per A_V with substantial scatter.

The bluest stars in $[\text{F410M}] - [\text{F466N}]$ ¹⁴ are seen at the edge of the cloud. Figure 2 shows the location of these bluest ($[\text{F410M}] - [\text{F466N}] < -0.45$ mag) stars. The most extinguished stars, which are the reddest in most colors but are bluest in colors involving F466N, are primarily seen along the outskirts of the cloud. Figure 4(a) shows stars color-coded by $[\text{F187N}] - [\text{F405N}]$ color. We use $[\text{F187N}] - [\text{F405N}]$ color as a consistency check: this color is very well correlated with both $[\text{F182M}] - [\text{F212N}]$ and $[\text{F212N}] - [\text{F410M}]$ color in panel (b), indicating that the trend seen in panel (c) is not caused by F410M. The interior of the cloud appears relatively blue in Figure 4(a) because only low-extinction stars are detected in the shorter-wavelength filters, and we plot only stars with detections in all six filters in this figure. Figure 4(b) highlights that colors not involving the F466N filter are consistent with extinction.

4.2. The F466N Recombination Lines are Fainter than Expected

The diffuse emission circumscribing The Brick, seen in F405N and F466N in Figure 1, is composed primarily of $\text{Br}\alpha$ (F405N) and $\text{Pf}\beta$ plus $\text{H}\epsilon$ (F466N) emission. Figure 3 shows where these lines reside with respect to the transmission profiles of the filters. There are no other expected sources of

¹³ We used the CT06_MWGC extinction curve from the `dust_extinction` package because it was implemented in that package, was appropriate for the Galactic Center, and covered the range of filters used in this work. The data used by CT06 come from Lutz (1999) and Indebetouw et al. (2005).

¹⁴ We use the bracket notation, e.g., $[\text{F466N}]$, to indicate a magnitude measurement. $[\text{F410M}] - [\text{F466N}]$ indicates a difference in magnitudes, i.e., a flux ratio or a color. Negative colors are blue, positive colors are red, by convention.

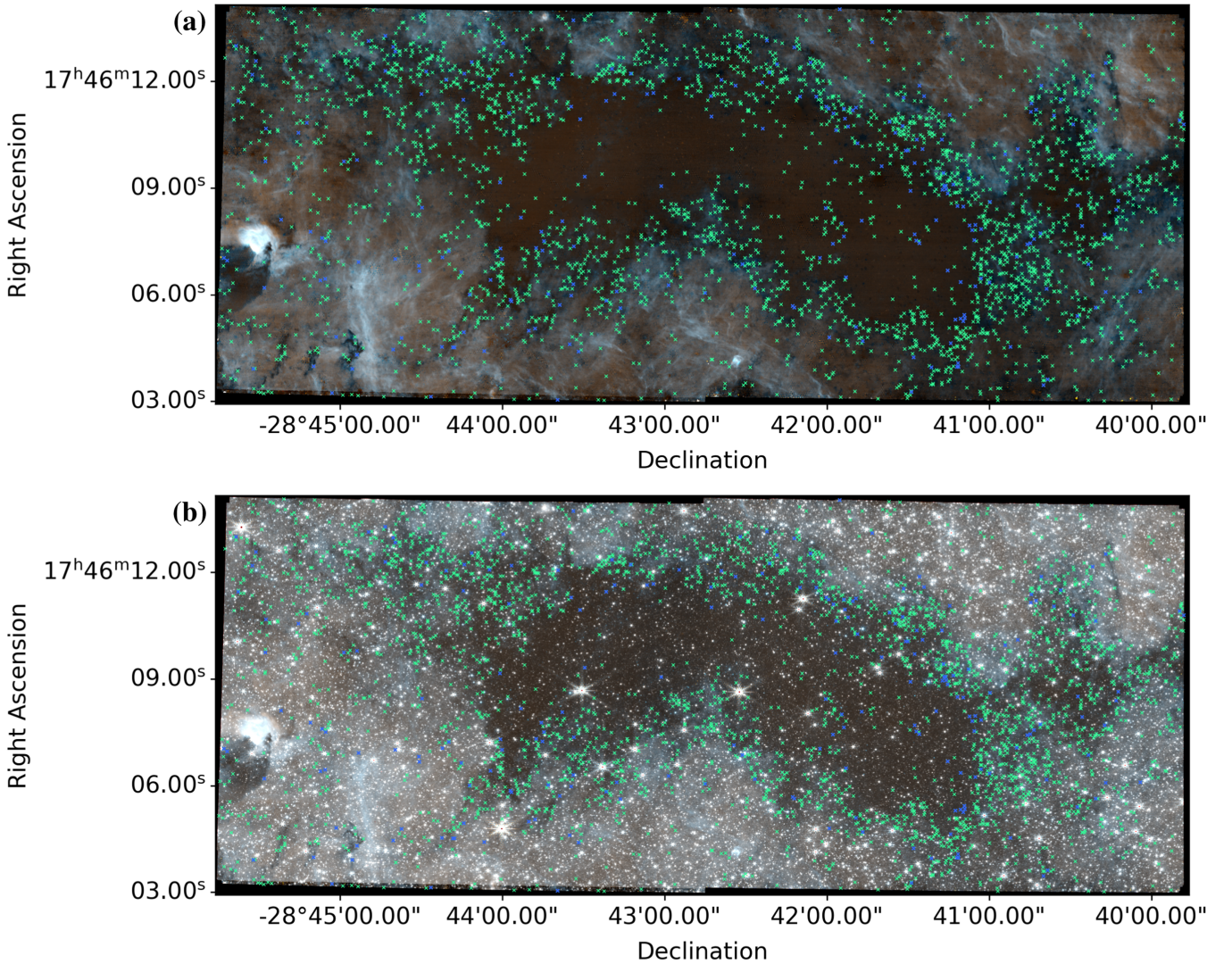


Figure 2. Stars with blue $[F410M] - [F466N]$ colors ($[F410M] - [F466N] < -0.45$ mag in green and < -1.45 mag in blue) shown with X's on (a) the star-subtracted RGB image and (b) the not-star-subtracted image. Note that decl. is on the x -axis, contrary to convention.

emission in this band, as there are no known features of polycyclic aromatic hydrocarbons in the $4\text{--}5\ \mu\text{m}$ range and free-free emission is expected to be weaker by $\sim 100\times$ in the narrow bands.

The ratio of hydrogen recombination lines is governed by simple rules under the assumption of Case B recombination, which is expected at moderate densities. The expected ratio of $\text{Pf}\beta/\text{Br}\alpha$ under Case B recombination at electron temperature $T_e \sim 5000\text{--}10^4\ \text{K}$ is $R_{\text{Pf}\beta/\text{Br}\alpha} = 0.202$ (Storey & Hummer 1995). The ratio of $\text{Pf}\beta + \text{H}\alpha$, the sum of the two lines in F466N, to $\text{Br}\alpha$ is $R_{(\text{Pf}\beta + \text{H}\alpha)/\text{Br}\alpha} = 0.234$. The average foreground extinction toward the CMZ (Launhardt et al. 2002; Nogueras-Lara et al. 2021) is $A_V = 30$. Using a CT06 extinction curve, in the absence of narrow spectral features, the ratio above rises to $R_{(\text{Pf}\beta + \text{H}\alpha)/\text{Br}\alpha}(A_V = 30) = 0.269$. At greater extinction, this ratio (which is equivalent to $[F405N] - [F466N]$ color) is expected to rise (become redder). However, contrary to this expectation, we see the $[F405N] - [F466N]$ color becoming more negative (bluer) along the edge of The Brick (Figures 1 and 2). We are therefore seeing that, in regions of greater extinction, the ratio is the inverse of what is expected from dust extinction alone.

4.2.1. CO Absorption of the F466N Recombination Lines

There are additional absorption processes that affect only the F466N filter. The F466N filter covers both CO gas and ice features (we will discuss these further in Sections 4.3 and 4.4), and therefore we expect the $[F405N] - [F466N]$ color to be more negative than the theoretical Case B recombination value if CO ice is present along the line of sight. We observe this decrease: the edges of the molecular cloud appear brown in Figure 1, indicating a relative deficiency in the F466N filter compared to regions farther from the molecular cloud.

To assess whether the absorption is caused by CO gas or ice, we model the absorption caused by CO. Figure 3(b) shows a CO line profile modeled assuming local thermodynamic equilibrium (LTE) conditions for a column density of $N(\text{CO}) = 5 \times 10^{16}\ \text{cm}^{-2}$, temperature $T = 50\ \text{K}$, and line width $\sigma = 5\ \text{km s}^{-1}$. This figure shows that there is a greater than $100\ \text{km s}^{-1}$ offset between the CO gas lines and the hydrogen recombination lines. The broadest line widths observed in the molecular gas are less than $20\ \text{km s}^{-1}$ (Henshaw et al. 2019), so CO lines are unlikely to strongly absorb the recombination line emission.

By contrast, CO ice produces broadband absorption that affects both the $\text{Pf}\beta$ and $\text{H}\alpha$ lines. Figure 3 shows CO and CO_2

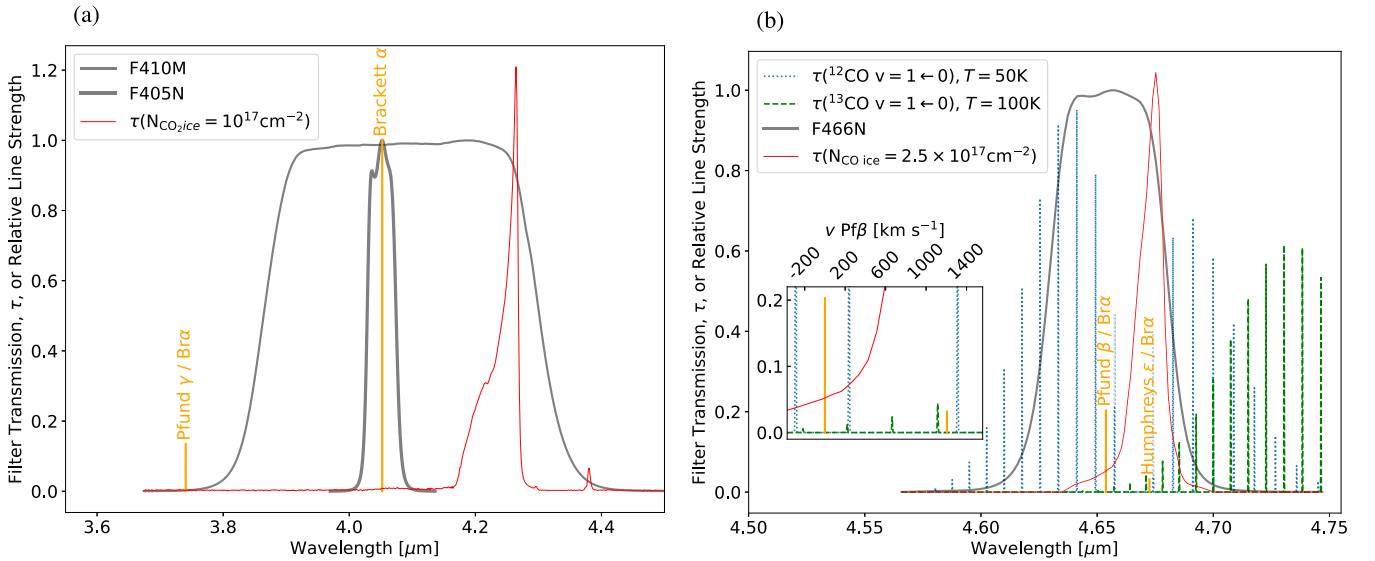


Figure 3. CO ice can absorb recombination line emission, but CO gas cannot. This figure shows the transmission curve, relative intensity of hydrogen recombination emission lines, and optical depth of CO gas absorption lines in selected NIRCcam long-wavelength filters: (a) F410M and F405N and (b) F466N. This is a schematic figure showing where lines and ice features appear and what their relative strengths are, but the amplitude scales are arbitrary: we selected column densities of CO such that the peak $\tau \approx 1$, while the inferred column densities are ~ 2 orders of magnitude greater. Both the F466N and F405N filters cover hydrogen recombination lines. We show these as orange stick spectra (i.e., they have no width), with peak levels set as the ratio of the emissivity of the labeled line to that of Br α under case B conditions for $n_e = 10^4 \text{ cm}^{-3}$ and $T = 10^4 \text{ K}$ (see Section 4.2). The CO gas, discussed in Section 4.3, overlaps extensively with the F466N filter. The optical depth of CO gas absorption τ is shown using a synthetic spectrum with $N(\text{CO}) = 5 \times 10^{16} \text{ cm}^{-2}$, $T = 50 \text{ K}$, and $\sigma = 5 \text{ km s}^{-1}$ (Section 4.3). Both ^{12}CO and ^{13}CO are shown with the same column density, but we expect $N(^{13}\text{CO}) \approx 25N(^{12}\text{CO})$ (e.g., Henkel et al. 1985). ^{13}CO is shown with a greater temperature, $T = 100 \text{ K}$, because at 50 K the lines near H $\nu\epsilon$ are too weak to appear in the figure. As shown in the inset in panel (b), the Pf β line lies between the CO $\nu = 1 \leftarrow 0$ $J = 1 \leftarrow 0$ and $J = 2 \leftarrow 1$ transitions ($\Delta v \approx 200\text{--}300 \text{ km s}^{-1}$), while H $\nu\epsilon$ is close to the $J = 0 \leftarrow 1$ transition ($\Delta v \approx 100 \text{ km s}^{-1}$). These lines would therefore require implausibly large broadening and/or Doppler shift to overlap. The red thin curves show optical depth of CO and CO $_2$ ice τ using Hudgins et al. (1993) transmission curves, which overlap with the recombination lines.

absorption profiles both with assumed $N(\text{CO}) = 10^{17} \text{ cm}^{-2}$. The CO ice profile overlaps significantly with both recombination lines in the F466N filter. We also model the CO $_2$ ice feature as a consistency check: if CO ice is present, CO $_2$ ice is also likely present, and therefore we verify that CO $_2$ ice would not undo the observed blue colors in [F405N] – [F466N]. The CO $_2$ ice, shown in panel (a), significantly overlaps with the F410M filter but has little overlap with the Br α line, confirming that CO $_2$ ice can be present without driving [F405N] – [F466N] toward the red.

Based on the observation that there is excess absorption of the diffuse F466N, and the modeling shown in Figure 3, we conclude that CO ice, and not CO gas, is absorbing Pfund β and Humphreys ϵ emission.

4.3. CO Gas

As shown in Figure 3, the ^{12}CO lines in the F466N band can produce significant absorption against stellar continuum light. In this section, we evaluate whether CO gas can produce the observed stellar colors. We already saw in Section 4.2 that CO gas is unlikely to produce selective extinction of Pf β +H $\nu\epsilon$. We find here that CO gas contributes to, but does not dominate, the total absorption in F466N.

We model this absorption as a function of temperature, column density, and line width assuming LTE conditions. Details of this modeling are given in an associated Jupyter notebook, COFundamentalModeling.ipynb, that can be found in the associated GitHub repository. The model implementation is in the `pyspeckit-models` package, which implements models compatible with `pyspeckit` (Ginsburg et al. 2022). We used transition and level tables

from the exomol database (Tennyson et al. 2016) derived from Li et al. (2015) using Yurchenko et al. (2018) as an implementation reference.

Figure 5 shows example optical depth spectra overlaid on the transmission profile of the F466N filter. The $\nu = 1 \leftarrow 0$ and $J = 4 \leftarrow 3$, $3 \leftarrow 2$, $2 \leftarrow 1$, $1 \leftarrow 0$ R-branch transitions and the $\nu = 1 \leftarrow 0$ $J = 0 \leftarrow 1$ P-branch transition all lie within the range where F466N has $>50\%$ of peak transmission (we use \leftarrow in the transition names to indicate that these are absorption lines). The maximum absorption in this filter occurs for temperatures between 10 and 20 K, while we expect gas temperatures near 50–100 K (Immer et al. 2012; Ginsburg et al. 2016; Krieger et al. 2017). At greater temperatures, a large fraction of CO molecules are in states that only produce transitions outside of the F466N band, reducing the absorption for a fixed assumed column density. It is possible that some of the CO gas is at moderate densities ($n(\text{H}_2) \lesssim 10^4 \text{ cm}^{-3}$) and therefore is subthermally excited, which would concentrate the CO molecules into the lower- J levels, thereby reducing the effect of high gas temperature. Nevertheless, the LTE models shown in Figure 5 capture the range of expected behavior.

We model the CO gas absorption for the expected range of line width and column density in the Galactic Center. For narrow line widths, such as those caused by thermal broadening at $T < 100 \text{ K}$, the absorption is negligible. In the Galactic Center, there is significant Doppler broadening that is generally attributed to turbulence. The total line width in the cloud may range from $\sigma \sim 5$ to 20 km s^{-1} (Henshaw et al. 2019). CO column densities will span the full range from effectively zero (since CO is destroyed by UV at $A_V \lesssim 2$) to a few $\times 10^{19} \text{ cm}^{-2}$ (Rathborne et al. 2015) assuming $X_{\text{CO}} = 10^{-4}$. In our observations, we detect stars at wavelengths short of $2 \mu\text{m}$

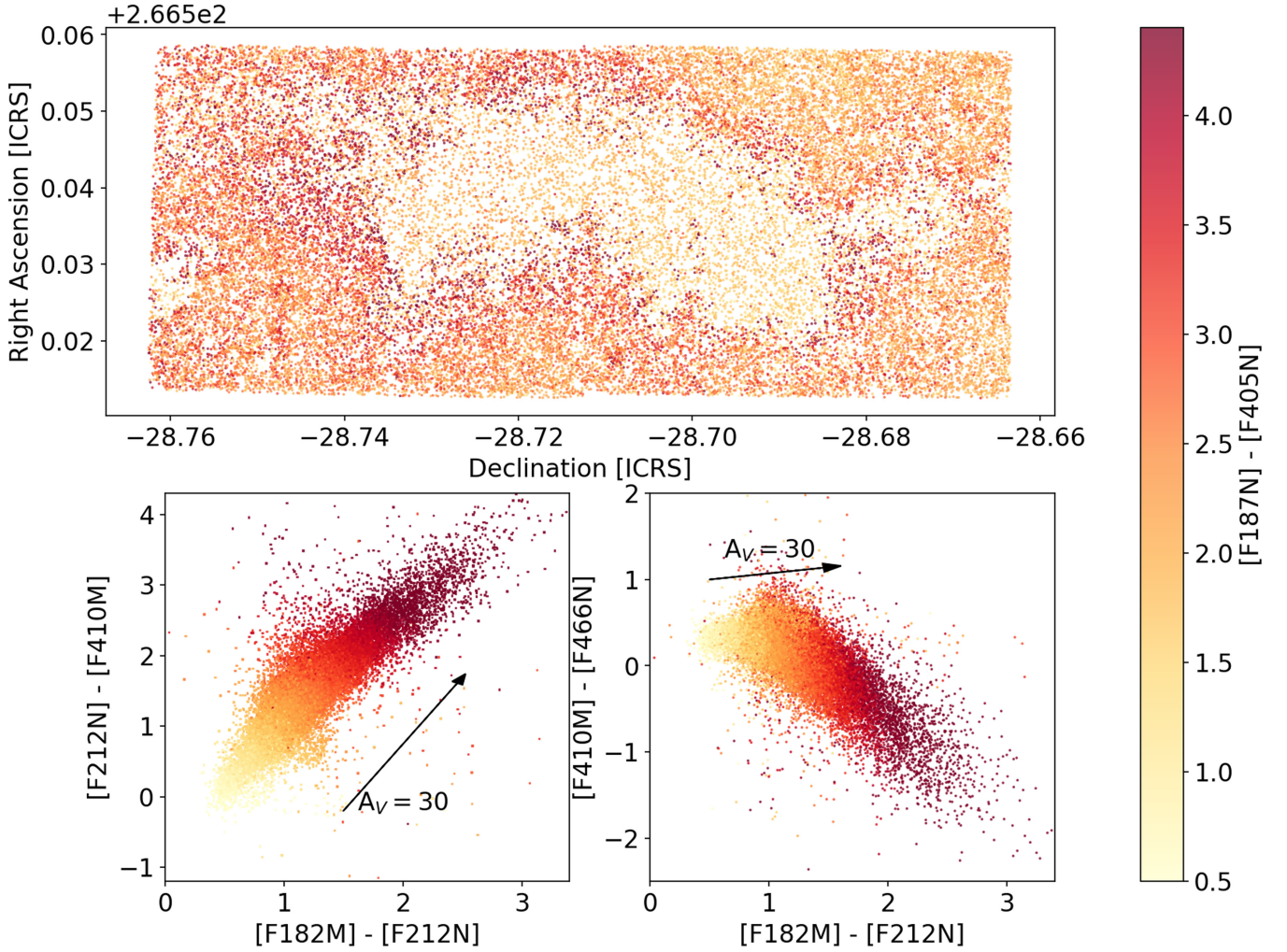


Figure 4. (a) Location of the 34,150 stars with detections in all six bands that met the quality criteria specified in Section 3.3 and that have $[F410M] < 15.4$ mag. Note that decl. is on the x -axis. (b) Comparison of $[F182M] - [F212N]$ to $[F212N] - [F410M]$ color. (c) Comparison of $[F182M] - [F212N]$ to $[F410M] - [F466N]$ color. An extinction vector $A_V = 30$ using the CT06 curve is overlaid, corresponding to about 1 magnitude of $[F182M] - [F212N]$ color excess. In (b), the extinction vector parallels the stars in the CCD, while in (c), the dust extinction vector points in a different direction: the $[F410M] - [F466N]$ color becomes bluer, rather than redder, with increasing extinction. The correlation between the color bar and each of the colors in (b) indicates that all of these colors align with dust extinction. We adopted a sequential color map to emphasize the most extinguished sources, which show up as dark red in the displayed $[F187N] - [F405N]$ colors. The color map uses $[F187N] - [F405N]$ to demonstrate that all observed colors not involving F466N exhibit reddening consistent with dust extinction).

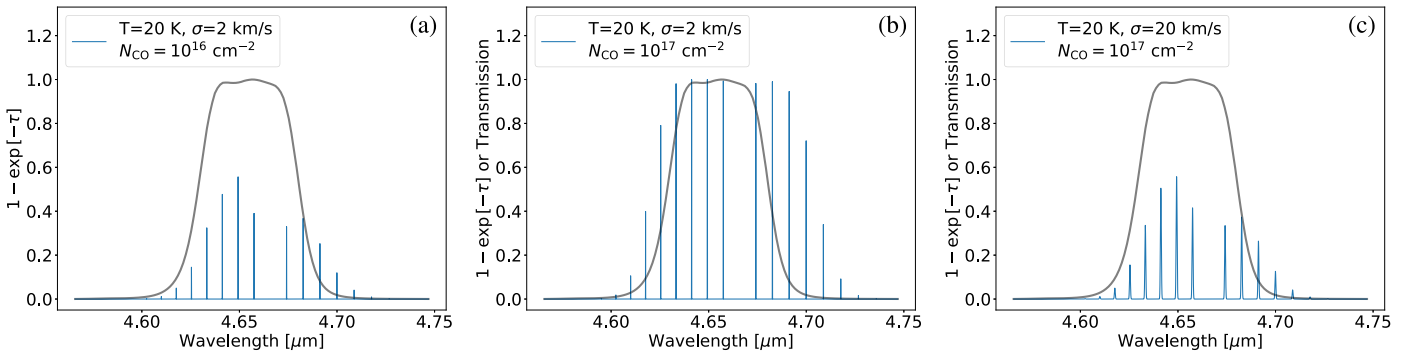


Figure 5. Example spectra showing the optical depth of gas-phase $^{12}\text{CO } v = 1 \leftarrow 0$ absorption superposed on the transmission spectrum of the F466N filter for a variety of physical conditions. The thick black curve in each case shows the transmission function of the F466N filter. The thin blue curves show the absorbed light fraction $1 - e^{-\tau}$. (a) The effect of this absorption for a low column density ($N(\text{CO}) = 1 \times 10^{16} \text{ cm}^{-2}$ or $N(\text{H}_2) = 1 \times 10^{20} \text{ cm}^{-2}$ for a typical CO abundance of $X_{\text{CO}} = 10^{-4}$). (b) $N(\text{CO}) = 10^{17} \text{ cm}^{-2}$ ($N(\text{H}_2) = 10^{21} \text{ cm}^{-2}$). (c) Transmission for CO column density 10^{17} cm^{-2} ($N(\text{H}_2) = 1 \times 10^{21} \text{ cm}^{-2}$) but with a broader line, illustrating that more of the band is absorbed but the peak optical depth is lower. We model low column densities to illustrate the behavior that affects the majority of stars in our sample, which are at relatively low column density, and to highlight the effects of gas temperature on the lines that are excited. The modeled column densities here fall significantly short of the peak column in The Brick, $N(\text{H}_2) \approx 5 \times 10^{23} \text{ cm}^{-2}$, but panel (b) captures the behavior at greater column densities: the line optical depths are large, so the lines are saturated. At greater column densities, there is very modest optical depth broadening, but qualitatively even extremely high column density resembles that model spectrum.

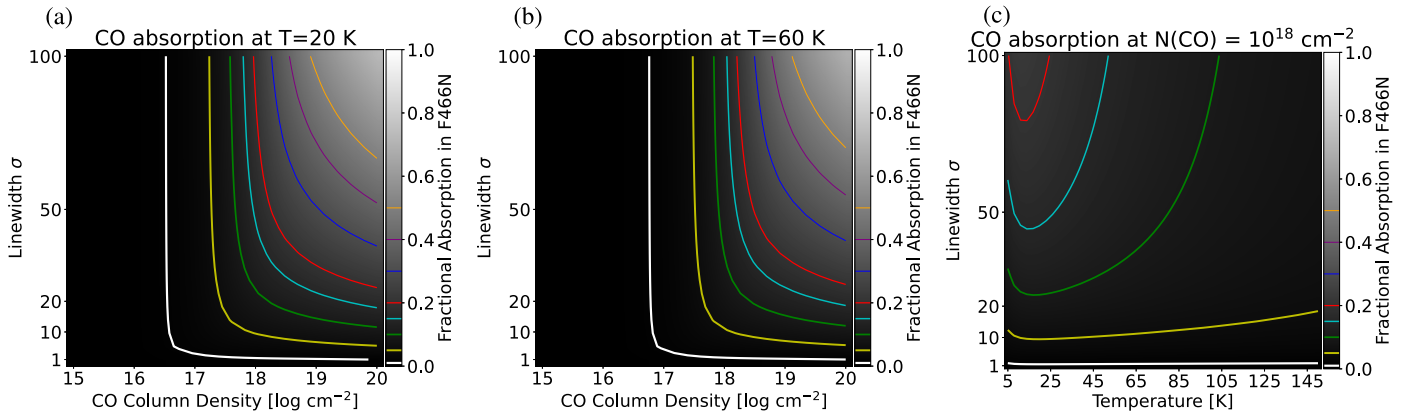


Figure 6. The fractional absorption by gas-phase CO $\nu = 1-0$ absorption within the F466N band for 20 K (left), 60 K (middle), and at a fixed column density $N_{\text{CO}} = 10^{18} \text{ cm}^{-2}$ (right). The grayscale shows the fractional absorption as labeled in the color bar; an absorption of 1.0 implies that no photons are received in the band. Colored lines are placed at levels = [0.01, 0.05, 0.1, 0.15, 0.2, 0.3, 0.4, 0.5] with colors = [white, yellow, green, cyan, red, blue, purple, orange], respectively, to help guide the eye. These curves occur in order from bottom to top and the line widths progress from thick to thin. These levels correspond to magnitude differences $\Delta m = [0.011, 0.056, 0.114, 0.176, 0.242, 0.387, 0.555, 0.753]$.

only at intermediate column densities, most likely below $A_V < 80 \text{ mag}$ ($N(\text{H}_2) < 10^{23} \text{ cm}^{-2}$), since dust extinction hides the stellar continuum at greater column density at the current level of sensitivity.

Figure 6 summarizes the modeling results. Given the plausible range of column density and line width, the total CO gas absorption in F466N may range from $\sim 1\%$ to at most $\lesssim 20\%$.

At the column densities where the absorption is easily detectable (fractional absorption $\gtrsim 0.1$ results in a change in magnitude $\Delta m \gtrsim 0.1$; green line in Figure 6), change in line width dominates over the change in column density or temperature. The foreground Galactic disk clouds, which have narrow lines, produce relatively little absorption; we therefore argue that intervening material between us and the Galactic Center is not primarily responsible for the blue [F410M] – [F466N] color of the stars. These models also imply that, even at very extreme column densities ($N_{\text{CO}} > 10^{19} \text{ cm}^{-2}$), “normal” Galactic disk clouds with $\sigma < 10 \text{ km s}^{-1}$ will produce minimal CO absorption in the F466N band, while typical clouds in the Galaxy Center and Galactic bar with $\sigma \sim 10\text{--}50 \text{ km s}^{-1}$ will produce readily detectable absorption. However, even for very broad lines ($\sigma = 50 \text{ km s}^{-1}$) at high column ($N_{\text{CO}} \sim 10^{19.5} \text{ cm}^{-2}$), CO gas produces $\lesssim 1$ magnitude ($< 50\%$) of absorption in the F466N band.

4.4. CO Ice Absorption

While we show above that CO gas can produce a substantial amount of absorption, the observed absorption depths reach levels difficult to explain with gas alone. Figure 6 shows that CO column densities $N(\text{CO}) > 10^{19.5} \text{ cm}^{-2}$, implying $N(\text{H}_2) > 3 \times 10^{23} \text{ cm}^{-2}$, are required to explain the $\gtrsim 2$ magnitudes of F466N absorption shown in Figure 4. Such high column densities are rare in The Brick (Rathborne et al. 2014a), occurring primarily in the inner regions (see their Figure 2) and in dense cores (Walker et al. 2021), while the high-extinction and high-CO-absorption stars we detect are primarily in the outskirts (Figure 2). Stars behind these high column densities would be too extinguished to detect in the shorter-wavelength band; the highest extinction we report in Section 4.4.2 is $A_V \sim 80 \text{ mag}$, or $N(\text{H}_2) \sim 10^{23} \text{ cm}^{-2}$. Additionally, in Section 4.2, we showed that CO gas is unlikely to absorb recombination lines. We

therefore examine the possibility that ice absorption is responsible for the observed F466N deficits.

There is evidence that The Brick contains some ice, but also that CO is not entirely frozen out. Pure CO ice forms at low temperatures, $T < 20 \text{ K}$ (Hudgins et al. 1993). The average dust temperature in The Brick is close to 20 K (Tang et al. 2021), so it is probable that some of the volume of The Brick is cold enough to freeze CO. The Brick exhibits signs of substantial freezeout in its center based on gas observations (Rathborne et al. 2014b), but still has substantial gas-phase CO detected (Ginsburg et al. 2016; Rigby et al. 2016; Eden et al. 2020). It is likely that much of the observed gas-phase CO is on the cloud surface, while further into the interior, CO is more completely frozen out.

4.4.1. CO Ice Modeling

To model CO ice absorption, we convolved a given filter transmission curve with a synthetic stellar model spectrum. We began with a 4000 K PHOENIX stellar atmosphere (Husser et al. 2013) as the base model, then examined the fractional flux lost in the F466N band as a function of CO column density. We retrieved optical constants for pure CO ice and CO mixed with OCS and CH_4 in a 20:1 ratio from Hudgins et al. (1993) via the JPL Optical Constants Database.¹⁵ We do not know which ice mixture is most appropriate for our data, so we chose to show all available laboratory mixtures in which CO was the primary constituent. We also considered the possibility that CO is embedded in other ices (e.g., H_2O and CH_3OH , Pontoppidan et al. 2003; Boogert et al. 2008), but found little practical difference from pure CO ice when using the optical constants of Hudgins et al. (1993) and Rocha et al. (2016).

Figure 7 shows the effects of CO ice absorption¹⁶: at $N(\text{CO}) \approx 10^{19} \text{ cm}^{-2}$, we expect $\approx 0.5\text{--}1 \text{ mag}$ of absorption from the ice band. The greatest observed column density within The Brick, based on dust emission observations from the Atacama Large Millimeter/submillimeter Array (ALMA) with $\sim 3''$ resolution, is $N(\text{H}_2) \sim 5 \times 10^{23} \text{ cm}^{-2}$ (Rathborne et al. 2014a), which implies an upper limit on the ice column density

¹⁵ <https://ocdb.smce.nasa.gov/page/toc>

¹⁶ Figure 7(a) includes the F470N filter, which we have not used in this work, to caution other JWST users that there may be significant, albeit weaker, CO absorption in this filter.

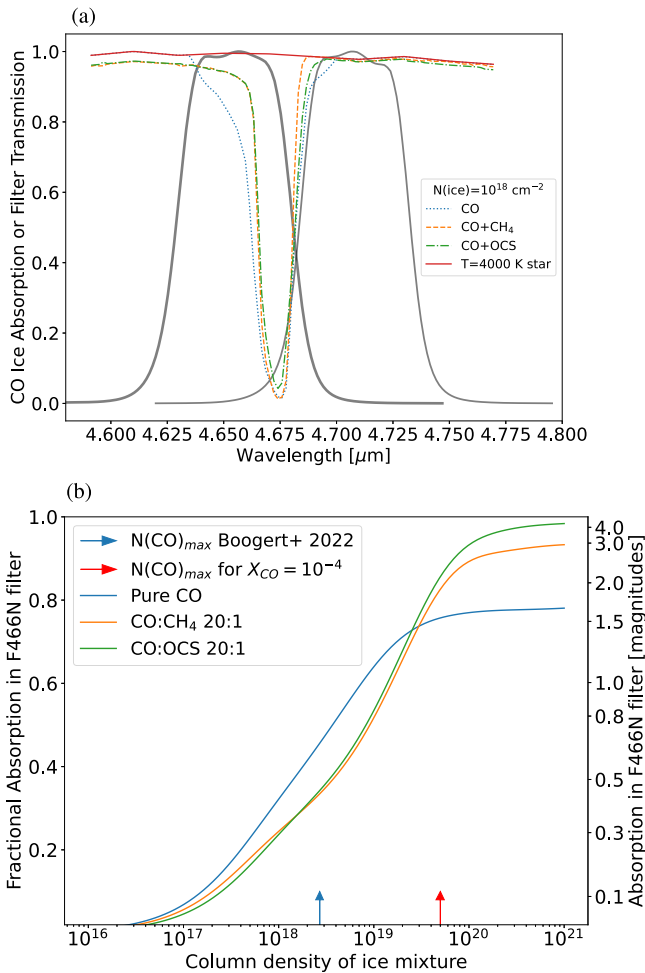


Figure 7. (a) Overlap of the transmission profiles of the F466N and F470N filters with CO ice absorption models superimposed on a PHOENIX 4000 K stellar photosphere model. The absorption profiles are produced using Hudgins et al. (1993) opacity measurements. (b) The expected absorption as a function of column density in the F466N band for three different CO ices. The absorption is given as a fractional value on the left and in magnitudes on the right. The arrows show the highest observed column density of CO ice from the Boogert et al. (2022) sample of high-mass young stellar objects and the maximum possible CO column density assuming a CO abundance with respect to H₂ of 10⁻⁴ given the observed column density in The Brick (but see Section 5.1 for a discussion of this assumption).

$N(\text{CO}) < 5 \times 10^{19} \text{ cm}^{-2}$ if we assume the CO/H₂ ratio is 10⁻⁴ and the gas-to-dust mass ratio is 100. If all of the CO is frozen out into pure CO ice, in the highest column-density line of sight, the absorption in F466N could just about reach 1.2 mag (~65%).

Figure 8 shows similar plots for the F405N and F410M filters for CO₂ ice to demonstrate that CO₂ ice can have some effect, but less so than CO, on our observed colors.

4.4.2. CO Ice as a Function of Extinction

We compared the inferred extinction to the CO ice column to obtain a coarse estimate of how CO ice varies with A_V . We use [F182M] – [F212N] color to estimate A_V by using the CT06 extinction curve, which we justify by comparing to ground-based GALACTICNUCLEUS colors in Appendix A.

To measure the CO absorption, we used the [F410M] – [F466N] color. Figure 4(c) shows that the [F410M] – [F466N] color becomes bluer at greater extinction. We calculated the

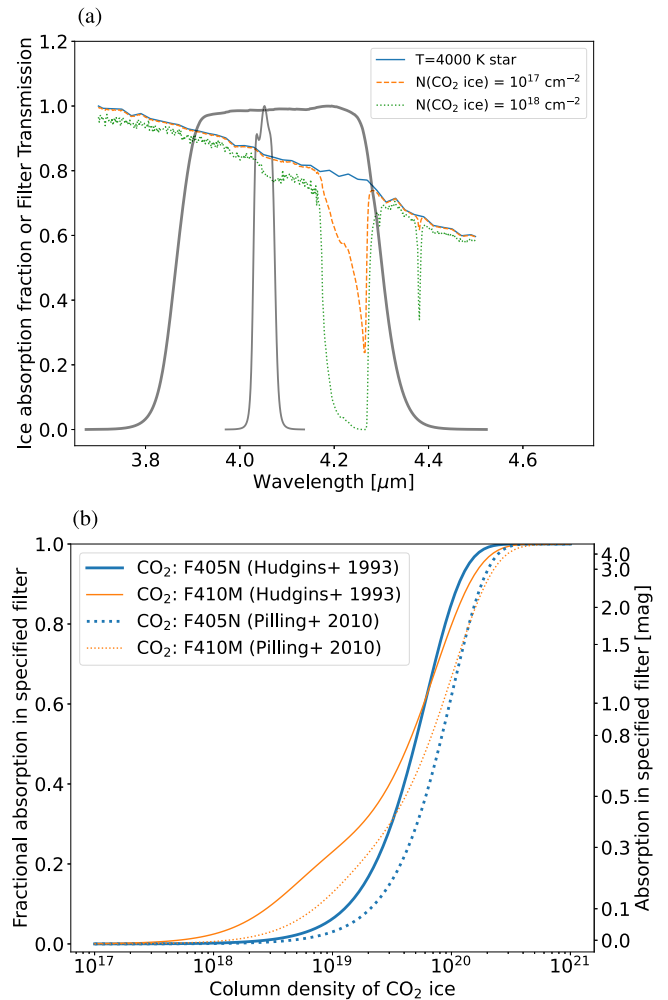


Figure 8. (a) Overlap of the transmission profiles of the F405N and F410M filters with CO₂ ice absorption models superimposed on a PHOENIX 4000 K stellar photosphere model. The absorption constants are for pure CO₂ ice from Hudgins et al. (1993) via the Optical Constants Database. (b) The expected absorption as a function of column density in the F405N and F410M bands. The absorption is given as a fractional value on the left and in magnitudes on the right.

absorption from pure CO ice in the F466N band to obtain a mapping from $N(\text{CO})$ to [F410M] – [F466N] color. We dereddened our measured [F410M] – [F466N] color using the A_V computed above with the CT06 extinction curve. Note that the assumed extinction curve introduces a strong systematic uncertainty: using a Fritz et al. (2011) extinction curve would reduce the estimated A_V by a factor of 1.8. Figure 9 shows the resulting $N(\text{CO})$ as a function of A_V . Note that this curve assumes that 100% of the deficit in the [F466N] band is produced by ice, which is an upper limit and likely an overestimate because CO gas (Section 4.3) also contributes, especially at low column density.

The red curve in Figure 9 shows the maximum possible CO at each A_V adopting standard values of $N(\text{H}_2) = 2.21 \times 10^{21} A_V$ (Güver & Özel 2009) and CO abundance relative to hydrogen $X_{\text{CO}} = 10^{-4}$. Some of the data points reside above this curve, suggesting that one or both of these assumptions may be incorrect, which we will evaluate further in Section 5.1.

While there is a good overall correlation between $N(\text{CO})$ and A_V , the dispersion at any given A_V is large, greater than one order of magnitude. Such a large scatter indicates a wide range

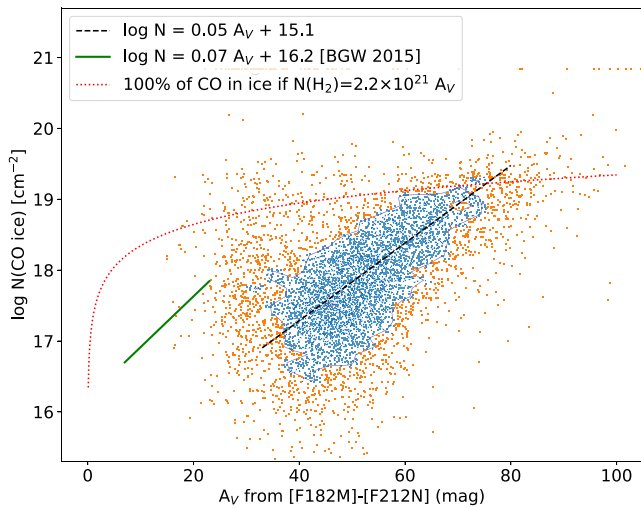


Figure 9. $N(\text{CO ice})$ vs. A_V . The black dashed line is shown as a representative typical value; it is not a fit to the data. The green solid line is from Boogert et al. (2015, Figure 7). The red dotted line shows the CO column density obtained by converting $N(\text{CO}) = N(\text{H}_2)/10^4$. A_V is computed from $[F182M] - [F212N]$ color using the CT06 extinction law. We caution that the x -axis is subject to systematic uncertainty from the choice of extinction curve; using the Fritz et al. (2011) curve instead of CT06 would compress the x -axis by a factor of 1.8. Additionally, $N(\text{CO ice})$ is calculated assuming 100% of the F466N deficit is produced by ice, not gas, while gas certainly contributes to the absorption, especially at lower column density (see Section 4.3). Statistical errors are limited to $\sigma(\log N(\text{CO})) \lesssim 0.17$ dex and $\sigma(A_V) \lesssim 4.4$ mag, which come from the selections imposed on the catalog (we include only stellar measurements with $\sigma < 0.1$ mag) and a simple linear propagation of error for $N(\text{CO})$.

of conditions, with many lines of sight containing little CO at the lowest observed A_V .

5. Discussion

5.1. CO Produces F466N Absorption

The CO ice models can qualitatively explain most of the observed F466N deficits. However, neither the gas nor ice models appear to quantitatively explain the most deeply absorbed sources. In both the gas and ice absorption cases, it is possible to achieve substantial absorption in the F466N band, enough to be easily detected, but less than the 1–2 mag seen in Figure 4 if typical CO abundance and gas-to-dust ratios are used.

One possible explanation lies in our assumptions about how to convert column densities between dust, molecular hydrogen, and CO: if the CO/H₂ ratio is greater than the assumed 10^{-4} , or the gas-to-dust ratio is less than 100 (e.g., Giannetti et al. 2017), the total CO column could be greater. Increasing the CO abundance or decreasing the gas-to-dust ratio, both of which are plausible because gas in the CMZ has a higher metallicity than the solar neighborhood, would both have the effect of shifting the red dashed line upward in Figure 9. These changes would therefore increase the maximum allowed CO abundance and explain the large observed F466N absorption.

5.2. Ice Freezeout and Gas Thermodynamics

The presence of significant quantities of CO ice in The Brick highlights the fact that the dust is significantly colder than the gas. Gas temperatures in the CMZ generally (Ginsburg et al. 2016; Krieger et al. 2017), and The Brick specifically (Johnston

et al. 2014), are observed to be high, $T \gtrsim 50$ K, and in many locations $T > 100$ K. Freezing of pure CO into ice is expected to occur at dust temperatures $T \lesssim 20$ K, though CO can be integrated into H₂O and CH₃OH ices that freeze out at higher temperatures ($T \gtrsim 80$ K; Garrod & Herbst 2006; Boogert et al. 2015). The dust temperatures observed in The Brick have been in the range $T \sim 20$ –30 K, albeit at lower resolution (Marsh et al. 2016; Tang et al. 2021), which is somewhat too warm for pure CO freezeout but cold enough to freeze other molecules. However, dust temperature measurements are biased toward warmer dust, since it is brighter, so it is likely that colder dust is present deep inside The Brick.

Both an excess of CO in Galactic Center gas and freezeout during gravitational collapse may result in a change in the effective equation of state of the gas. In the dense molecular medium ($n \gtrsim 10^3$ cm⁻³) that comprises The Brick, CO is the dominant gas-phase coolant (Ginsburg et al. 2016). If the CO abundance is greater than in the solar neighborhood (Section 5.1), we expect more efficient cooling in the lower-density outskirts of CMZ clouds. By contrast, as the clouds collapse to greater density, there may be a point at which the CO has frozen out to the point that it is no longer the dominant coolant, but where the densities are still too low for dust to be an efficient coolant. We suggest that systematic variations in the cooling function as a function of density or column density should be explored in future simulations of CMZ cloud thermodynamics like those in Clark et al. (2013).

5.3. Broader Implications and Future Applications

The prevalence of CO ice in our own Galactic Center hints that ice is likely widespread in galactic centers generally. At least in the local universe, then, JWST observations using the long-wavelength narrowband filters should carefully treat CO absorption in addition to extinction effects. Our Figure 9 gives an empirical tool to link extinction and ice, though we caution that the large scatter demonstrated in that plot limits the usefulness of the linear relation given in its legend.

The easy detection of ices in the F466N narrowband filter also creates opportunities to better understand dust and ice in the interstellar medium and to understand cloud structures. While NIRSpect will be capable of studying hundreds of stars with ice absorption in detail, NIRCcam observations can easily measure tens of thousands of sightlines simultaneously, enabling detailed correlation analyses like those shown in Figure 9. By adding comparable-resolution gas observations from ALMA, it should be possible to trace the freezeout of CO from gas to ice in detail. With a few other bands, such as F300M and F335M, it will be possible to track H₂O and CH₃OH ice and determine when and how much CO is incorporated into H₂O ice, which freezes at a substantially higher temperature.

The overlap of the CO ice feature with Pf β +H $\nu\epsilon$ also opens the possibility of making ~ 0.1 resolution maps of CO ice absorption against the diffuse ionized emission. From the Pa α /Br α ratio, we can determine the dust extinction on a per-pixel basis, which will enable specific measurement of CO ice absorption from the now known Br α /Pf β ratio. Since the CO ice feature affects the Pf β line, but CO gas does not, this approach will also allow us to distinguish whether ice or gas is the dominant absorber on most sightlines.

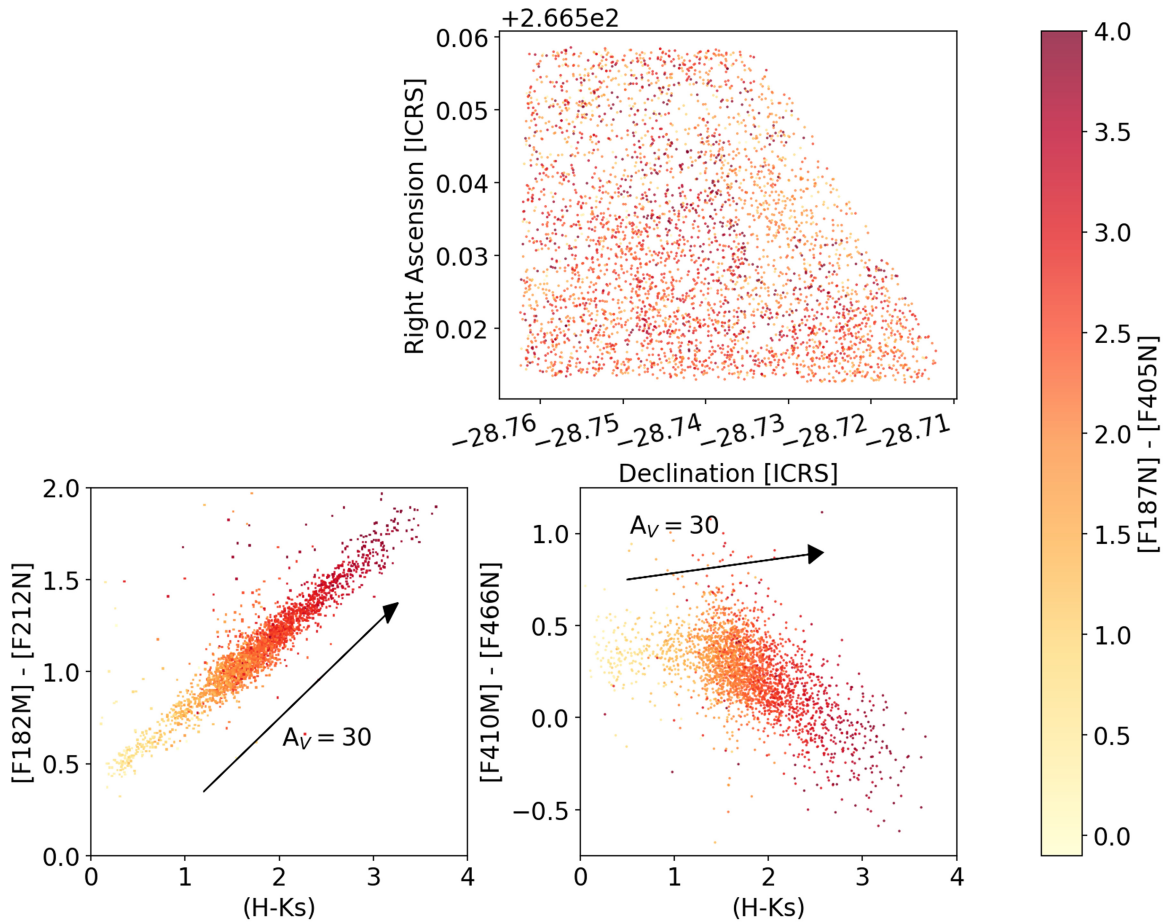


Figure 10. Spatial plot (top) and color–color diagrams (bottom) for the subset of our sample cross-matched with the GALACTICNUCLEUS survey (Nogueras-Lara et al. 2021). The left CCD shows our [F182M] – [F212N] color against the GN ($H - K_s$) color, demonstrating that there is very good correlation between these colors and justifying the use of [F182M] – [F212N] as an extinction estimator. The right CCD shows our [F410M] – [F466N] against GN ($H - K_s$) color, demonstrating that the F466N deficit is anticorrelated with ($H - K_s$) color.

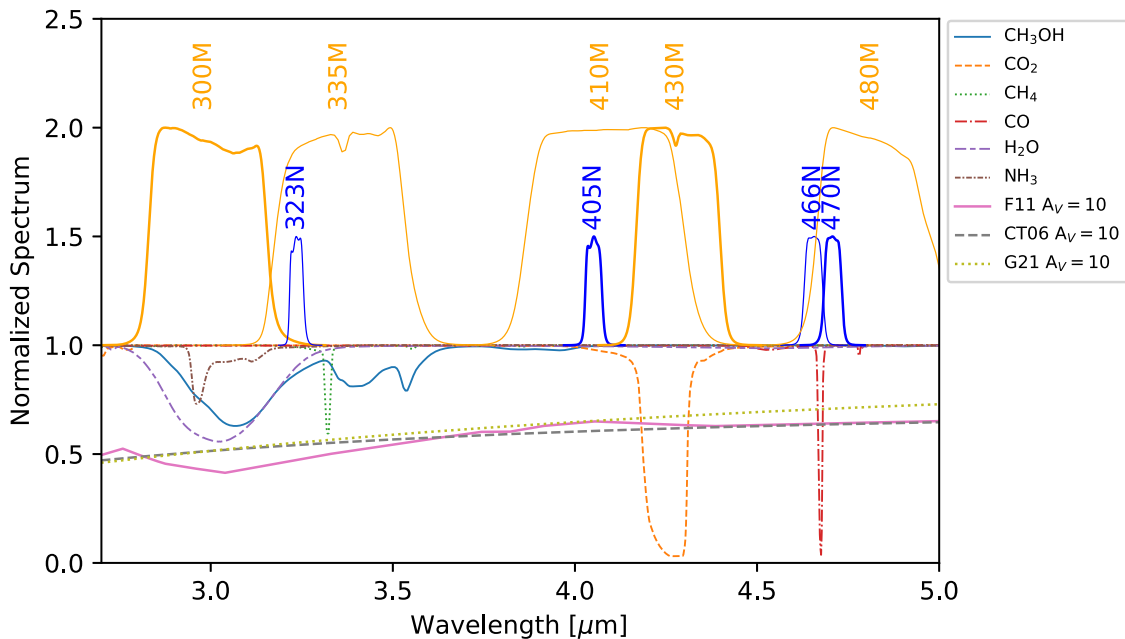


Figure 11. Plot of ice absorption and JWST NIRCcam filter profiles. The normalized filter profiles are shown as the positive features above 1.0; all are peak-normalized. Orange colors are medium-band, blue are narrowband. The blue ice absorption profiles from several ices are shown in the bottom part of the plot; each ice is plotted with a column density $N(\text{ice}) = 10^{18} \text{ cm}^{-2}$. For many of these molecules, this is an unrealistically high column density, but it is helpful to illustrate where absorption occurs. The lower panel shows extinction profiles for three different models: Chiar & Tielens (2006), Fritz et al. (2011), and Gordon et al. (2021).

6. Conclusions

We report observations of G0.253 + 0.016, an infrared dark cloud known as “The Brick,” with JWST’s NIRCам in narrowband filters. We produce a cross-matched photometric catalog using the `crowdsourc` package. We find 377,236 unique sources, of which 56,146 are detected in all six photometric bands.

In this first publication on these data, we show that there is significant absorption toward stars in the F466N band, which is caused by CO ice and gas. We argue that ice is predominant along most sightlines and provide modeling results to show the effect of ice and gas absorption on this and other JWST filters. While CO absorption is a suitable explanation for the observed F466N absorption, the quantities of both ice and gas required to produce the observed absorption are in some tension with the observed line-of-sight column density. This result indicates that the standard abundance of CO ($X_{\text{CO}} = 10^{-4}$) and/or the dust-to-gas ratio (10^{-2}) is too low for the Galactic Center environment.

Acknowledgments

We thank the referee for a helpful and very detailed report, particularly on their review of labeling conventions and figure clarity. We thank Eddie Schlafly and Andrew Saydjari for their assistance with `crowdsourc` technical issues. A.G. acknowledges support from STSCI grant JWST-GO-02221.001-A, and from the NSF through AST 2008101, AST 220651, and CAREER 2142300. C.B. gratefully acknowledges funding from the National Science Foundation under Award Nos. 1816715, 2108938, 2206510, and CAREER 2145689, as well as from the National Aeronautics and Space Administration through the Astrophysics Data Analysis Program under Award No. 21-ADAP21-0179 and through the SOFIA archival research program under Award No. 09 0540. X.L. acknowledges support from the National Natural Science Foundation of China (NSFC) through grant No. 12273090, and the Natural Science Foundation of Shanghai (No. 23ZR1482100). J.D.H. gratefully acknowledges financial support from the Royal Society (University Research Fellowship; URF \R1 \221620).

Appendix A

Comparison to GALACTICNUCLEUS

The GALACTICNUCLEUS (GN) near-infrared survey (Nogueras-Lara et al. 2019, 2021) partially overlaps with the targeted field of view presented here. GN has better resolution than VVV and therefore presents a better match to our data set, but we chose to use VVV as our primary astrometric reference in Section 3 because GN covers only about half of the southern field we observed. The greater resolution and sensitivity of GN, however, mean that it is more appropriate for photometric comparison.

To verify our use of narrowband and medium-band filters in our extinction measurements, we cross-matched our catalog to the GN catalog and produced color–color diagrams using the GN ($H - K_s$) color as a more typical tracer of extinction. We found the closest match in our catalog to each GN source and kept all sources with a separation of $< 0''.2$. In the field in which GN overlaps our observations, there are a total of 16,021 GN sources and 69,918 sources detected in all three of our short-wavelength bands. Of the GN sources, 14,557 sources have JWST sources within $0''.2$, of which 6844 pass quality criteria






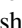




specified in Section 3.4 for all JWST short-wavelength filters and 3958 pass quality criteria for all six filters. Figure 10 shows that we reproduce the same qualitative result as shown in Figure 4 with these data. This plot demonstrates that our color used to measure extinction in the JWST data, $[F182M] - [F212N]$ color, is well correlated with the standard ground-based ($H - K_s$) color.

Appendix B

Ice-affected Filters

We demonstrate in this paper that ice absorption affects at least the F466N filter in Galactic Center photometry. We highlight the narrowband and medium-band NIRCам filters that are potentially affected by ices in Figure 11. This plot was made using optical constants from the JPL Optical Constants Database¹⁷ using the `icemodels` package.¹⁸ This figure provides a quick-look tool for determining how likely an observation in a given filter is to be affected by ice absorption, and therefore is a good first step to check if one encounters unexpected colors in the long-wavelength NIRCам bands.

ORCID iDs

Adam Ginsburg  <https://orcid.org/0000-0001-6431-9633>
 Ashley T. Barnes  <https://orcid.org/0000-0003-0410-4504>
 Cara D. Battersby  <https://orcid.org/0000-0002-6073-9320>
 Alyssa Bulatek  <https://orcid.org/0000-0002-4407-885X>
 Savannah Gramze  <https://orcid.org/0000-0002-1313-429X>
 Jonathan D. Henshaw  <https://orcid.org/0000-0001-9656-7682>
 Desmond Jeff  <https://orcid.org/0000-0003-0416-4830>
 Xing Lu  <https://orcid.org/0000-0003-2619-9305>
 E. A. C. Mills  <https://orcid.org/0000-0001-8782-1992>
 Daniel L. Walker  <https://orcid.org/0000-0001-7330-8856>

References

- An, D., Ramírez, S. V., Sellgren, K., et al. 2011, *ApJ*, 736, 133
 Ao, Y., Henkel, C., Menten, K. M., et al. 2013, *A&A*, 550, A135
 Bally, J., Rathborne, J. M., Longmore, S. N., et al. 2014, *ApJ*, 795, 28
 Boogert, A. C. A., Brewer, K., Brittain, A., & Emerson, K. S. 2022, *ApJ*, 941, 32
 Boogert, A. C. A., Gerakines, P. A., & Whittet, D. C. B. 2015, *ARA&A*, 53, 541
 Boogert, A. C. A., Pontoppidan, K. M., Knez, C., et al. 2008, *ApJ*, 678, 985
 Brasseur, C. E., Rogers, T., Donaldson, T., et al. 2020, in ASP Conf. Ser. 522, *Astronomical Data Analysis Software and Systems XXVII*, ed. P. Ballester et al. (San Francisco, CA: ASP), 97
 Bushouse, H., Eisenhamer, J., Dencheva, N., et al. 2023, JWST Calibration Pipeline, v1.11.1, Zenodo, doi:10.5281/zenodo.8099867
 Chiar, J. E., & Tielens, A. G. G. M. 2006, *ApJ*, 637, 774
 Chiar, J. E., Tielens, A. G. G. M., Whittet, D. C. B., et al. 2000, *ApJ*, 537, 749
 Clark, P. C., Glover, S. C. O., Ragan, S. E., Shetty, R., & Klessen, R. S. 2013, *ApJL*, 768, L34
 Eden, D. J., Moore, T. J. T., Currie, M. J., et al. 2020, *MNRAS*, 498, 5936
 Federrath, C., Rathborne, J. M., Longmore, S. N., et al. 2016, *ApJ*, 832, 143
 Fritz, T. K., Gillessen, S., Dodds-Eden, K., et al. 2011, *ApJ*, 737, 73
 Garrod, R. T., & Herbst, E. 2006, *A&A*, 457, 927
 Giannetti, A., Leurini, S., König, C., et al. 2017, *A&A*, 606, L12
 Ginsburg, A., & Gramze, S. 2023, keflavich/brick-jwst-2221: Resubmission to *ApJ*, resubmission 20230903, Zenodo, doi:10.5281/zenodo.8313307
 Ginsburg, A., Henkel, C., Ao, Y., et al. 2016, *A&A*, 586, A50
 Ginsburg, A., Sipińcz, B. M., Brasseur, C. E., et al. 2019, *AJ*, 157, 98
 Ginsburg, A., Sokolov, V., de Val-Borro, M., et al. 2022, *AJ*, 163, 291
 Gordon, K. D., Misselt, K. A., Bouwman, J., et al. 2021, *ApJ*, 916, 33
 Günay, B., Burton, M. G., Afşar, M., & Schmidt, T. W. 2020, *MNRAS*, 493, 1109

¹⁷ <https://ocdb.smce.nasa.gov/page/toc>

¹⁸ <https://github.com/keflavich/icemodels/>

- Günay, B., Burton, M. G., Afşar, M., & Schmidt, T. W. 2022, *MNRAS*, **515**, 4201
- Güver, T., & Özel, F. 2009, *MNRAS*, **400**, 2050
- Henkel, C., Guesten, R., & Gardner, F. F. 1985, *A&A*, **143**, 148
- Henshaw, J. D., Ginsburg, A., Haworth, T. J., et al. 2019, *MNRAS*, **485**, 2457
- Henshaw, J. D., Kruijssen, J. M. D., Longmore, S. N., et al. 2020, *NatAs*, **4**, 1064
- Henshaw, J. D., Krumholz, M. R., Butterfield, N. O., et al. 2022, *MNRAS*, **509**, 4758
- Henshaw, J. D., Longmore, S. N., & Kruijssen, J. M. D. 2016, *MNRAS*, **463**, L122
- Hudgins, D. M., Sandford, S. A., Allamandola, L. J., & Tielens, A. G. G. M. 1993, *ApJS*, **86**, 713
- Husser, T. O., Wende-von Berg, S., Dreizler, S., et al. 2013, *A&A*, **553**, A6
- Immer, K., Menten, K. M., Schuller, F., & Lis, D. C. 2012, *A&A*, **548**, A120
- Indebetouw, R., Mathis, J. S., Babler, B. L., et al. 2005, *ApJ*, **619**, 931
- Jang, D., An, D., Sellgren, K., et al. 2022, *ApJ*, **930**, 16
- Johnston, K. G., Beuther, H., Linz, H., et al. 2014, *A&A*, **568**, A56
- Jones, P. A., Burton, M. G., Cunningham, M. R., et al. 2012, *MNRAS*, **419**, 2961
- Kauffmann, J., Pillai, T., & Zhang, Q. 2013, *ApJL*, **765**, L35
- Krieger, N., Ott, J., Beuther, H., et al. 2017, *ApJ*, **850**, 77
- Kruijssen, J. M. D., Dale, J. E., & Longmore, S. N. 2015, *MNRAS*, **447**, 1059
- Launhardt, R., Zylka, R., & Mezger, P. G. 2002, *A&A*, **384**, 112
- Li, G., Gordon, I. E., Rothman, L. S., et al. 2015, *ApJS*, **216**, 15
- Lis, D. C., & Carlstrom, J. E. 1994, *ApJ*, **424**, 189
- Lis, D. C., Carlstrom, J. E., & Keene, J. 1991, *ApJ*, **380**, 429
- Lis, D. C., & Menten, K. M. 1998, *ApJ*, **507**, 794
- Lis, D. C., Menten, K. M., Serabyn, E., & Zylka, R. 1994, *ApJL*, **423**, L39
- Lis, D. C., Serabyn, E., Zylka, R., & Li, Y. 2001, *ApJ*, **550**, 761
- Longmore, S. N., Rathborne, J., Bastian, N., et al. 2012, *ApJ*, **746**, 117
- Lutz, D. 1999, in *ESA Special Publication, The Universe as Seen by ISO*, ed. P. Cox & M. Kessler, Vol. 427 (Netherlands: ESA-SP), 623
- Lutz, D., Feuchtgruber, H., Genzel, R., et al. 1996, *A&A*, **315**, L269
- Marsh, K. A., Ragan, S. E., Whitworth, A. P., & Clark, P. C. 2016, *MNRAS*, **461**, L16
- Mills, E. A. C., Butterfield, N., Ludovici, D. A., et al. 2015, *ApJ*, **805**, 72
- Mills, E. A. C., Ginsburg, A., Immer, K., et al. 2018, *ApJ*, **868**, 7
- Moneti, A., Cernicharo, J., & Pardo, J. R. 2001, *ApJL*, **549**, L203
- Moultaka, J., Eckart, A., & Schödel, R. 2009, *ApJ*, **703**, 1635
- Nogueras-Lara, F., Schödel, R., Gallego-Calvente, A. T., et al. 2019, *A&A*, **631**, A20
- Nogueras-Lara, F., Schödel, R., Neumayer, N., & Schultheis, M. 2021, *A&A*, **647**, L6
- Perrin, M. D., Long, J., Sivaramakrishnan, A., et al. 2015, *WebbPSF: James Webb Space Telescope PSF Simulation Tool*, Astrophysics Source Code Library, ascl:1504.007
- Petkova, M. A., Kruijssen, J. M. D., Kluge, A. L., et al. 2023, *MNRAS*, **520**, 2245
- Pillai, T., Kauffmann, J., Tan, J. C., et al. 2015, *ApJ*, **799**, 74
- Pontoppidan, K. M., Fraser, H. J., Dartois, E., et al. 2003, *A&A*, **408**, 981
- Rathborne, J. M., Longmore, S. N., Jackson, J. M., et al. 2014a, *ApJL*, **795**, L25
- Rathborne, J. M., Longmore, S. N., Jackson, J. M., et al. 2014b, *ApJ*, **786**, 140
- Rathborne, J. M., Longmore, S. N., Jackson, J. M., et al. 2015, *ApJ*, **802**, 125
- Rigby, A. J., Moore, T. J. T., Plume, R., et al. 2016, *MNRAS*, **456**, 2885
- Rocha, W. R. M., Pilling, S., de Barros, A. L. F., et al. 2016, arXiv:1609.04684
- Rodríguez, L. F., & Zapata, L. A. 2013, *ApJL*, **767**, L13
- Saito, R. K., Hempel, M., Minniti, D., et al. 2012, *A&A*, **537**, A107
- Schlafly, E. F. 2021, *crowdsourc: Crowded field photometry pipeline*, Astrophysics Source Code Library, ascl:2106.004
- Storey, P. J., & Hummer, D. G. 1995, *MNRAS*, **272**, 41
- Tang, Y., Wang, Q. D., & Wilson, G. W. 2021, *MNRAS*, **505**, 2377
- Tennyson, J., Yurchenko, S. N., Al-Refaie, A. F., et al. 2016, *JMoSp*, **327**, 73
- Walker, D. L., Longmore, S. N., Bally, J., et al. 2021, *MNRAS*, **503**, 77
- Walker, D. L., Longmore, S. N., Bastian, N., et al. 2016, *MNRAS*, **457**, 4536
- Yurchenko, S. N., Al-Refaie, A. F., & Tennyson, J. 2018, *A&A*, **614**, A131